





cambridge.org/mrf

Tzichat M. Empliouk¹ , Petros I. Bantavis², Christos I. Koltsidas³,
Theodoros N. F. Kaifas¹ and George A. Kyriacou¹ 

¹Department of Electrical and Computer Engineering, Democritus University of Thrace, Xanthi, Greece; ²Greenerwave, Paris, 75002, France and ³Ericsson, Standards & Technology-HW Research, Kista, Sweden

Research Paper

Cite this article: Empliouk TM, Bantavis PI, Koltsidas CI, Kaifas TNF, Kyriacou GA (2023). Ultra-Wideband Six-Port Network Miniaturization—Matching. *International Journal of Microwave and Wireless Technologies* **15**, 1676–1688. <https://doi.org/10.1017/S1759078723000727>

Received: 03 January 2023
Revised: 16 May 2023
Accepted: 22 May 2023

Keywords:

meander microstrip lines; miniaturization of microwave circuits; six-port circuits

Corresponding author: George A. Kyriacou;
Email: gkyriac@ee.duth.gr

Abstract

In this paper, a new design approach for the six-port (SP) junction is introduced. The proposed design includes a generalized broadband matching and smooth miniaturization scheme and is extendable for any passive multiport structure. A multilayer technology and a microstrip to slot coupling operation are employed for the designed SP, which comprises power divider and three hybrid couplers. The conducted measurements of the constructed SP junctions validates the design approach. Optimal performance of the SP network in terms of miniaturization, bandwidth, and response accuracy were obtained for the 5G low band.

Introduction

Six-port (SP) networks have gained much popularity over the past decades due to its usability in many areas, including reflectometers, transceivers, and radio-source localization systems. Being a passive structure, it may offer ultra-wideband (UWB) characteristics, low complexity, and cost. In the field of microwave measurement systems, SP has been classically used as an alternative reflectometer or network analyzer for measuring the reflection coefficient amplitude and phase of a device under test [1–3]. In the area of microwave transceivers, SP-based technologies include direct conversion receivers for implementing software-defined radios (SDR) [4, 5], a direct conversion sensors for millimeter wave sensing applications [6, 7], Internet of Things applications [8], direct modulator for high data rate modulation schemes such as Quadrature Phase Shift Keying (QPSK) and Quadrature Amplitude Modulation (QAM) [9, 10], and high precision interferometer for radio frequency (RF) source localization and range calculation RF front end [11–13]. Beyond the UWB operation, the key characteristics that make SP junctions attractive for the aforementioned applications is its multiband and multimode functionalities, low power consumption, and compatibility in digital domain [14].

The prevailing challenges that arise in designing and developing SP junctions are to achieve compact size, UWB operation, and response accuracy. Indeed, the compact size eases the integration with other devices and systems (e.g Butler Matrix), a critical characteristic especially for 5G wireless communication where flexibility and space are important factors. UWB operation is also critical since the designed SP should maintain the desired response for a wide range of frequencies, augmenting and in many cases even enabling the needed functionality over the overlaid system. Response accuracy is also important in many cases as, for example, the amplitude accuracy in the q-points when SPs are operated as receivers or reflectometers. To answer those challenges, a huge research effort is devoted to the development of SP networks during the last decade. The most indicative attempts are summarized in Table 1 and reviewed next. Therein various characteristics including technology, size, BW, amplitude and phase response, accuracy of q-points, and the miniaturization technique are listed in comparison with the herein proposed technique.

In [15–19], SP networks implemented in planar technology are presented. Aiming at minimum size and maximum BW, 50% to 100% fractional bandwidth (FBW) is achieved in [15–17], but the designs suffer from poor performance in outputs, (S-parameters) amplitude (up to ± 3 dB), and phase (10° to 25°) variation. Fang et al. [18] attempted size reduction replacing $\lambda/4$ -lines using equivalent lines loaded by open stubs. Indeed, they achieved a reduction to 20% and $0.22\lambda^2$ footprint area, as compared to the conventional SP junction. However, this considerable size reduction came at the expense of FBW reduction to 25% and an amplitude deviation of ± 3.5 dB from the theoretical value of -6 dB. In [19], modified series diamond stubs were used along with power divider (PD) and branch line couplers, achieving 75% FBW and a size of about $0.34\lambda^2$. Multilayer technology is employed in [20–22], utilizing the multi-sectional approach for hybrid coupler (HC) and PD. Therein, an improvement in FBW from 120% to 150% is reported, but the compactness is partly sacrificed as the size is increased to

© The Author(s), 2023. Published by Cambridge University Press in association with the European Microwave Association. This is an Open Access article, distributed under the terms of the Creative Commons Attribution licence (<http://creativecommons.org/licenses/by/4.0>), which permits unrestricted re-use, distribution and reproduction, provided the original article is properly cited.

Table 1. Multilayer SP networks comparison

Work	OB (GHz)	I/MT	S (mm ²)/R (%)	NS (λ)	FA (λ^2)/(%)	FBW (%)	$IL_{Av} \pm \Delta A$ (dB)	PA	q-A
[20]	0.7–5.8	Stripline	130 × 150	1.4 λ × 1.62 λ	2.29/63	150	-7.5 ± 2	10°	-
[21]	2–8	Microstrip to stripline	128 × 98	2.13 λ × 1.63 λ	3.48/43	120	-7.2 ± 1.7	10°	-
[22]	2–8	Stripline	128 × 98	2.13 λ × 1.63 λ	3.48/43	120	-6.75 ± 1	-	-
[23]	3.6–10.4	Microstrip to slot	43 × 43	1 λ × 1 λ	1/83.5	94	-6.5 ± 2	-	-
[24]	3–5	Microstrip to stripline	12.7 × 13.2	0.17 λ × 0.18 λ	0.03/99.5	50	-6 ± 2	±45°	-
[25]	1–3	Microstrip/ML	32 × 34/79	0.21 λ × 0.23 λ	0.05/99.2	100	-10 ± 2	-	-
[26]	1–6	Microstrip to stripline /LTCC	30 × 30/63	0.35 λ × 0.35 λ	0.12/98	140	-7 ± 3	-	0.5–1.8/20°
[27]	22–28	SIW/Stacked SP	-/40	-	5.1/-	0.28	-7.5 ± 1.5	±12	-
This work	0.8–2.5	Microstrip to slot/EBM-ML	68 × 63/63	0.37 λ × 0.34 λ	0.13/98	103	-7 ± 1.9	18°	0.75–1.38/4°

Note: The acronyms are denoted as follow: OB, operating band; I, implementation; MT, miniaturization technique; S, size; R, reduction; NS, normalized size; FA, footprint area; $IL_{Av} \pm \Delta A$, average insertion loss with amplitude deviation; PA, phase accuracy; q-A, q-point accuracy.

about 3.48 λ^2 . A compromise between bandwidth (BW) and size is reported in [23], regarding a multilayer SP junction based on a microstrip to slot coupling. The achieved footprint area is 1 λ^2 , while the FBW reaches about 94%. Reasonable size reduction of two multilayer SP structures is reported in [24, 25]. Specifically, in [24], the authors were able to greatly reduce the size to 0.03 λ^2 retaining a 50% FBW but with large phase error ($\pm 45^\circ$). In [25], a 0.05 λ^2 footprint area and a 79% reduction in size compared to a planar design is achieved, while the FBW is retained to 100%. However, the right angles of the utilized rectangular meander lines in [25] cause significant loss in the outputs' amplitudes (10 ± 2 dB) and unknown phase deviations. The best performed SP compared to the SPs reported so far is found in [26] by Morena et al. Therein, a low temperature co-fired ceramic (LTCC) SP network was implemented using eight DuPont-943 substrate layers, achieving a size reduction of 63% with respect to the ordinary planar topology and a 140% FBW. A drawback of the approach in [26] is the high cost and complexity involved due to the implementation of LTCC technology. Recently, in [27], a multilayered substrate integrated waveguide SP junction with stacked SP components is introduced, achieving a size reduction of 40% but with limited FBW of 0.28.

In the work at hand, aiming to develop a compact plus wideband SP network covering the sub-6 GHz band of 5G (from UHF to 6 GHz as required by the usual SDR applications), multilayer technology is employed. In order for the compactness and wide BW to be accompanied with compliant S-parameters (accurate amplitude and phase response), we focus our attention on the transmission lines interconnecting the component devices (PD and HCs) constituting the SP. The required geometrical characteristics of those lines are properly calculated utilizing a broadband matching technique, which, in general, is applied to diode mixer design [28–30]. This technique is adopted and extended herein in order to formulate a generalized approach for matching passive components. Indeed, we contribute a new step-by-step design approach, which is carried out in two stages. At the first stage, the extended broadband matching (EBM) technique is used to match PD and HCs by estimating efficiently the geometrical characteristics of the interconnecting lines. Wide BW response and response accuracy is delivered by treating the interconnecting lines not as mere 50 Ω guides but as wideband, complex-to-complex, interconnecting,

distributed, two-port matching networks. At the second stage, compactness as well as wide BW results by appropriate reformation (smooth meandering) of the interconnecting transmission lines to properly fill a lot of the empty (unfunctional) spaces. Thus, a new SP network, with matched components and optimized interconnections, is delivered just combining the EBM and the smooth meandered line (ML) techniques. As a result, our effort compares favorable (with respect to miniaturization, the retaining of amplitude and phase accuracy, and low losses) with the state of the art (again summarized in Table 1). As shown in Table 1, the overall achieved size reduction for the designed SP junction is of the order of 63% for the 0.8 to 2.5 GHz band. Advantages of the proposed design approach is the reduced complexity compared to previous works, especially with respect to LTCC technology, the preservation of the UWB characteristics, and flexibility since it is easily applicable in multilayer as well as in planar configuration, and it is extendable to any multiport network. Summarizing, as depicted in Table 1, the technique elaborated herein exhibits optimal performance regarding size reduction, overall bandwidth, and response accuracy.

The rest of the paper is organized as follows. In section “UWB multilayer power divider and 3 dB hybrid coupler,” the initial design of HCs and PD is introduced, while in section “Extended broadband matching methodology of the hybrid coupler and power divider and footprint reduction,” the extended wideband matching methodology is presented along with the advantages provided by the use of MLs. Section “Design and implementation of six-port networks” presents the implemented SP networks, while their validation is given in section “Validation results.” Finally, in section “Conclusion,” conclusions are deduced.

UWB multilayer power divider and 3 dB hybrid coupler

Figure 1(a) depicts the SP network topology, which is used to perform vector measurements of two input RF signals (a_1 , a_2). For receiver applications, one of them is an unknown signal containing the desired information in both its phase and its amplitude, while the other one is a local oscillator signal. Conversely, for a source localization problem, the two signals could be the outputs of two

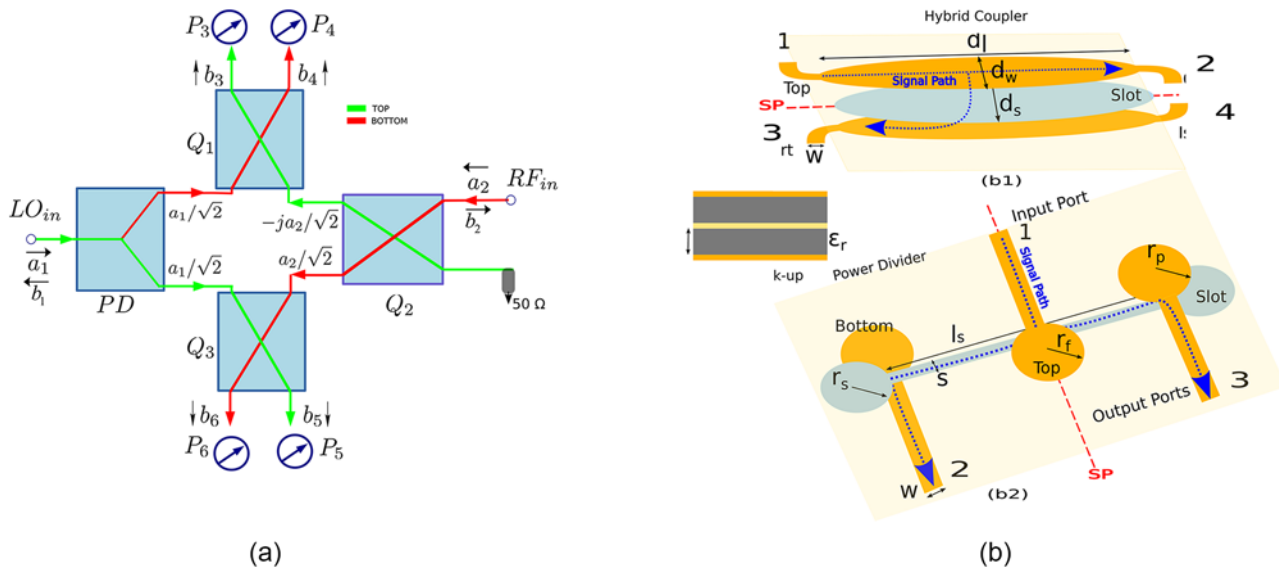


Figure 1. (a) Six port network topology. (b) Elliptically shaped multilayer 3 dB HC (b1-top) and multilayer PD (b2-bottom). SP denotes symmetry plane.

antenna elements. In both cases, the aim is to yield baseband voltages proportional to their amplitude ratio, a_1/a_2 , and their phase difference $a_1 - a_2$. As shown in Fig. 1(a), the SP topology comprises a PD and three HC. The components' multilayer structure is shown in Fig. 1(b). A microstrip to slot coupling is employed to equally divide incoming signals, with 0° phase shift for the case of PD and 90° for the HC. Since the overall performance of the SP junction depends on the performance of each of the PD and HC components, the first critical stage is to define their geometrical characteristics (Fig. 1(b)). Explicitly for the 90° HC based on [31], the multilayer topology as modified in our previous work [32] is considered. For the UWB-PD, the topology employed in [33–35] is adopted and modified in the present work.

Hybrid coupler

Referring to Fig. 1(b), the multilayer HC comprises three conductive layers interleaved with two dielectric layers. Elliptically shaped patches are printed on the top and bottom layers, which are coupled through an elliptical slot etched on the middle metallic (ground) layer. Thus, as shown in Fig. 1(b)2, a signal applied to input port is divided equally between output and coupled ports with a phase shift of -90° . Ideally there is no signal at the isolated port. Since there is a symmetry, the operation of the HC supports even and odd modes. Horizontal symmetry plane is applied with respect to ports 1 and 3 as shown in Fig. 1(b)1. In the odd mode, the currents on the two patches are antisymmetric, and thus the slot acts as a perfect electric conductor (PEC). Consequently, the HC geometry for the odd mode is treated as a common microstrip line of width w and characteristic impedance Z_{0o} . Conversely, in the even mode, the currents on the top and bottom patches are symmetric; hence, the slot acts as a perfect magnetic conductor. In turn, the HC geometry for the even mode is approximated by a slot line with characteristic impedance Z_{0e} and width d_s . The coupling mechanism and the operating BW are controlled by the widths d_w , d_s of the elliptical patch and slot, respectively, and the coupler length d_l . A detailed design methodology and the calculation of d_w , d_s , and d_l can be found in our previous work [32].

Power divider

Regarding the UWB-PD designs, we extend the PDs proposed in [33–35]. Herein, the output ports are rearranged in different layers in order to fit the multilayer structure and to achieve in-phase operation. Similar to HC, PD consists of three conductive layers interleaved with two dielectric layers (Fig. 1(b)). The input port and one output port are placed at the top layer and the second output port is placed at the bottom layer. Coupling between input and output ports is achieved in the middle layer via the slotline of length l_s and width s . The PD of Fig. 1(b)2 exhibits two transitions with transformation ratio n , which depends on the substrate characteristics (h , ϵ_r) and the frequency. The first transition occurs between the input port and the slotline, while the second occurs between the slotline and the output ports. A signal applied to port 1 is equally divided and coupled through the slotline at the first transition. The resulted signals, in turn, travel in opposite directions to the second transition where they are coupled to the output microstrip ports. Since the paths to the output ports are symmetric and in the same direction, a zero-phase difference results between them. In order to minimize reflections at input and output ports, throughout an UWB frequency range, the microstrip lines and the slotline are terminated with circular stubs of radius r_f , r_m , and r_s . Just as in [37], the microstrip and slot circular stubs act as capacitive and inductive elements, respectively.

Similar to HC, the PD of Fig. 1(b)2 supports even and odd mode operation. The output ports 2 and 3 are symmetrical, and hence the even and odd mode analysis is applicable to them. The related even–odd mode analysis follows [35], wherein a more general topology is studied since it includes a resistance isolating the two output ports. The isolation resistor is omitted herein in order to make the PD integration to the SP architecture more convenient. Hence, the even–odd mode analysis is quite similar, and the corresponding equivalent circuits and their mathematical expressions are repeated herein in their simplified form. When the odd mode is examined, the symmetry plane becomes a PEC and thus the voltage is zero. Subsequently, the input microstrip line is grounded through the electrical wall, and the input port sees a line terminated at short circuit (i.e., as a shortened stub). The equivalent circuit, as shown in Fig. 2(b), becomes a one-port network since the impedance at the

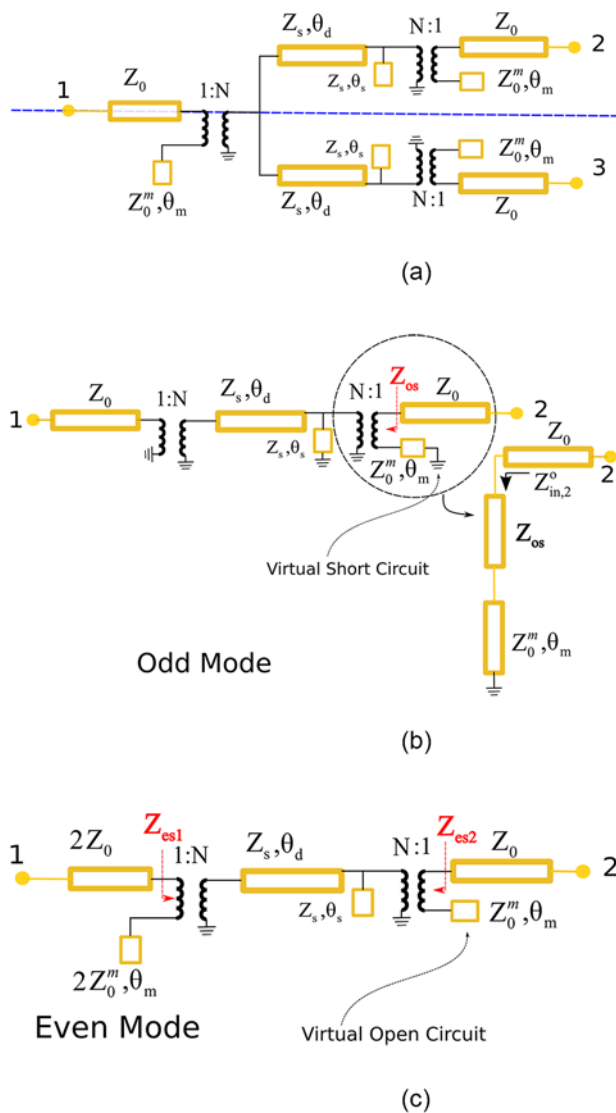


Figure 2. PD even and odd mode analysis: (a) equivalent circuit, (b) odd mode, and (c) even mode [35] but without an isolation resistor.

symmetry plane is zero. Referring to the encircled part of Fig. 2(b), the input impedance seen from the output port 2 is:

$$Z_{in,2}^o = Z_{os} + jZ_0^m \tan \theta_m \tag{1}$$

Z_0^m is the characteristic impedance of the microstrip circular stub, while Z_{os} is the impedance as seen at the slotline (through the N:1 transformer). For the particular case when $\theta_m = \theta_s = \pi/2$, then Z_{os} results to [35]:

$$Z_{os} = jn^2 Z_s \tan \theta_d \tag{2}$$

Z_s and θ_d are the characteristic impedance and the electrical length of the slotline, respectively. Notably, in Equation (2), the effect of the stub (Z_s, θ_s) disappears since its input impedance ($jZ_s \tan \theta_s$) tends to infinity for $\theta_s = \pi/2$. For wideband response, the slotline length should be equal to $\lambda_d/2$ ($\theta_d = \pi$ and $\tan \theta_d = 0$) [36]. Hence, Z_{os} can be omitted from Equation 1, yielding:

$$Z_{in,2}^o = jZ_0^m \tan \theta_m \tag{3}$$

For a good impedance matching, the above input impedance should be equal to the characteristic impedance of the microstrip line, $Z_{in,2}^o = Z_0$. For this purpose, Z_0^m and θ_m are tuned to secure $Z_{in,2}^o = Z_0 = 50 \Omega$. An optimal length for the microstrip circular stub of the proposed divider was found to be equal to $l_m = \lambda_m/14$.

When the even mode is enforced, two inphase signals are applied to the output ports. The symmetry plane becomes a perfect magnetic wall, and a virtual open circuit is placed at the symmetry axis. Hence, each bisected part of the PD becomes the two-port network shown in Fig. 2(c). The input impedance of the input port 1 is doubled ($2Z_0$), while the output ports exhibit an impedance equal to Z_0 . The absence of the isolation resistor does not change the analysis of the even mode with respect to [35] since this resistor is now terminated at open circuit. Thus, the input impedances of port 1 and port 2 adopted from [35], for the particular case when $\theta_m = \theta_s = \pi/2$, read:

$$Z_{in1}^e = \frac{n^2 Z_s (Z_{es1} + jZ_s \tan \theta_d)}{Z_s + jZ_{es1} \tan \theta_d} \tag{4}$$

$$Z_{in2}^e = \frac{n^2 Z_s (Z_{es2} + jZ_s \tan \theta_d)}{Z_s + jZ_{es2} \tan \theta_d} \tag{5}$$

Z_{es1}, Z_{es2} are the input impedances of the slotline at the two transitions, which are given as:

$$Z_{es1} = \frac{2Z_0}{n^2} \tag{6}$$

$$Z_{es2} = \frac{Z_0}{n^2} \tag{7}$$

Combining Equations (4)–(7), the appropriate characteristic impedance Z_s of the slotline is calculated.

The width and the length of the slotline are related to the transformation ratio n , which is initially estimated using expressions given in [33]. In turn, the slotline impedance is calculated as [37]:

$$Z_s = \frac{Z_m}{n^2} \tag{8}$$

$Z_m = 50 \Omega$ is the characteristic impedance of the microstrip line. With Z_s known, the width of the slotline s is estimated using closed form expressions given in [38]. After the estimation of the geometrical characteristics, the PD of Fig. 1(b)2 is designed and simulated using SIMULIA CST STUDIO. However, the initial design does not offer optimum performance in terms of insertion loss for output ports. The main reasons for this is the poor matching due to the removal of the isolation resistor. Thus, an optimization scheme is carried out, where the slot width is optimized to achieve the required results. Optimal values for the slot width s are between 0.2 and 0.35 mm, resulting in characteristic impedance of the slotline Z_s between 82 and 88 Ω and n between 0.75 and 0.78, which fulfills Equation (8). The above holds for the Rogers RO4003 substrate with $\epsilon_r = 3.55$ and thickness h equals to 0.508 mm.

Figure 3 depicts the S-parameters (left) and the phase difference of output ports (right) of the PD of Fig. 1(b)2. The insertion loss for the output ports varies from -3 to -4 dB at 0.8 to 5 GHz. As expected, there is a good matching at the input port where S_{11} is below -10 dB, but there is a mismatch regarding return loss and isolation at the output ports (note that $S_{22} = S_{33}$, due to symmetry). This is due to the fact that herein, compared to [35], the use of isolation resistor is avoided due to the placement of the microstrips at different (top and bottom) layers, which makes soldering difficult.

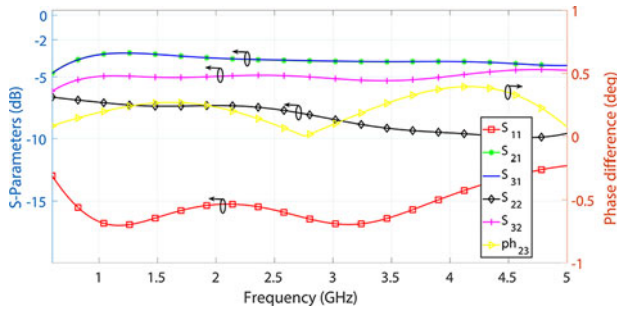


Figure 3. Simulated S-parameters (left) and the phase difference of output ports (right) of the power divider of Fig. 1(b)2.

However, the return loss and isolation mismatch at the output will not affect the overall performance of the SP network since output ports of PD are matched to the HC utilizing the wideband matching technique described in the next section. Explicitly, the adopted MLs provide the required good wideband matching even without the isolation resistor.

Extended broadband matching methodology of the hybrid coupler and power divider and footprint reduction

In the current section, the improved matching methodology for the HCs and PD and its interrelation with the miniaturization approach are stated. Broadband matching, applied in general to diode-mixers design [28–30], is adopted and extended herein for matching passive devices. In mixer design, although a wideband operation is sought, the diode impedance changes with time driven by the local oscillator large signal as well as with frequency. Thus, the diode impedance varies from a relatively low value $Z_{low} = Z_{on}$ at the on condition to a high value $Z_{high} = Z_{off}$ at the off condition. Wideband matching is achieved by estimating a hyperbolic mean value Z_m between Z_{low} and Z_{high} , which in turn is matched to the characteristic impedance of the feeding line (Z_0). In this manner, the diode impedance under local oscillator drive moves back and forth or around the center of the Smith chart ($Z_{in} = Z_m = Z_0$) versus time and frequency. Herein, the approach is carried out in two steps as shown in Fig. 4, where the basic principles of

real-to-complex and complex-to-complex matching are revealed. First, a length of series transmission line is added to the component to make the conductance at band edges equal to the inverse of the conductance at resonance. This is equivalent to matching (to the center of the Smith Chart) the hyperbolic mean of the whole band response using the same series transmission line. Second, the other element in the matching circuit is a shunt resonant transmission line shorted to ground to bring the band edge admittances together. The first part of the aforementioned procedure is depicted in Fig. 4(a) and is utilized to match PD or HCs to their respective ports (real-to-complex matching). The hyperbolic mean of the device’s response (using the $Z_{max(f)} = Z_{high}$ and $Z_{min(f)} = Z_{low}$ band-edge impedances) is computed and then matched using a properly calculated ($Z'_0, \theta' = \beta'l$) transmission line (Fig.4(a)). For the case of complex-to-complex matching, which is referred to the matching of interstage components as shown in Fig. 4(b) (for example, the PD with one of the HCs), we contribute here a generalization of the procedure stated in [28–30]. Herein the two hyperbolic means of the components named A and B are computed and then are complex conjugate matched together via the addition of a properly assessed interconnecting transmission line. Let us now focus on the second part of the wideband matching procedure. Although the hyperbolic mean may be driven to the center of the Smith chart, the band edge impedances remain relatively away. Ideally, the impedance locus versus frequency should run around a circle with minimum radius. A component is needed in order to bring the band edge admittances together. However, in the related references, a radial stub is employed to accomplish this goal. A stub operating as a series resonant circuit is best suited when the one edge impedance is inductive ($Im(Z_{low} > 0)$) and the other is capacitive ($Im(Z_{high} < 0)$). In this case, the resonant stub offers the opposite sign reactances, thus compensating the load imaginary parts. This is not the choice that we have made in the work at hand. Herein, the interconnecting transmission line is employed not only to match the hyperbolic mean but also to bring together the edge admittances. This is achieved by meandering the interconnecting line. Indeed, when a transmission line is meandered, it can be modeled as a semi-lumped circuit [39], where each ML unit cell is studied as transmission lines connected via shunt lossless components (the coupling inductors and capacitors). Conceiving the ML as inheriting shunt components opens the way to properly design

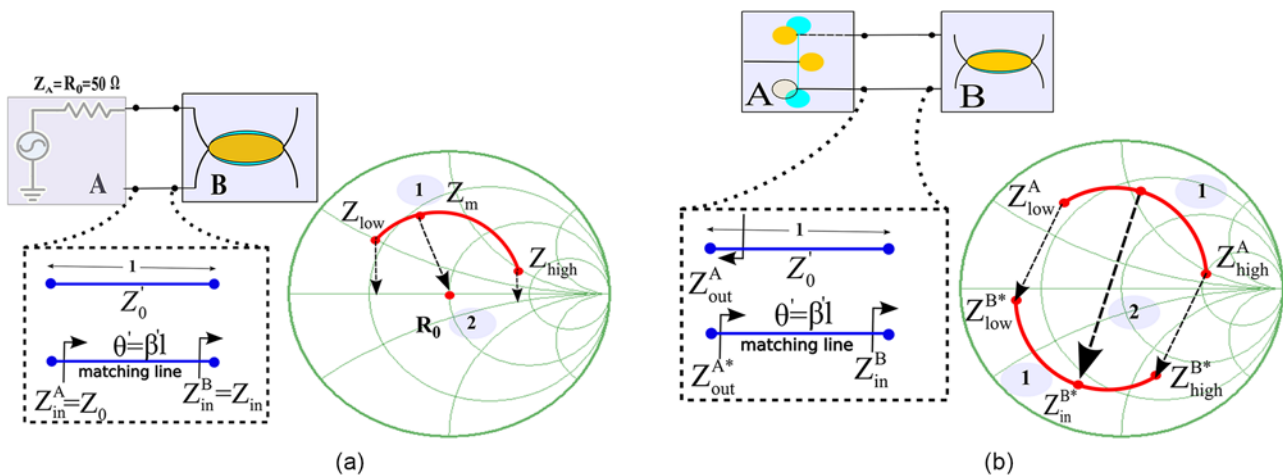


Figure 4. Wideband matching of passive devices. (a) Matching a component to Z_0 (real-to-complex matching). (b) Interstage matching of two components (complex-to-complex matching).

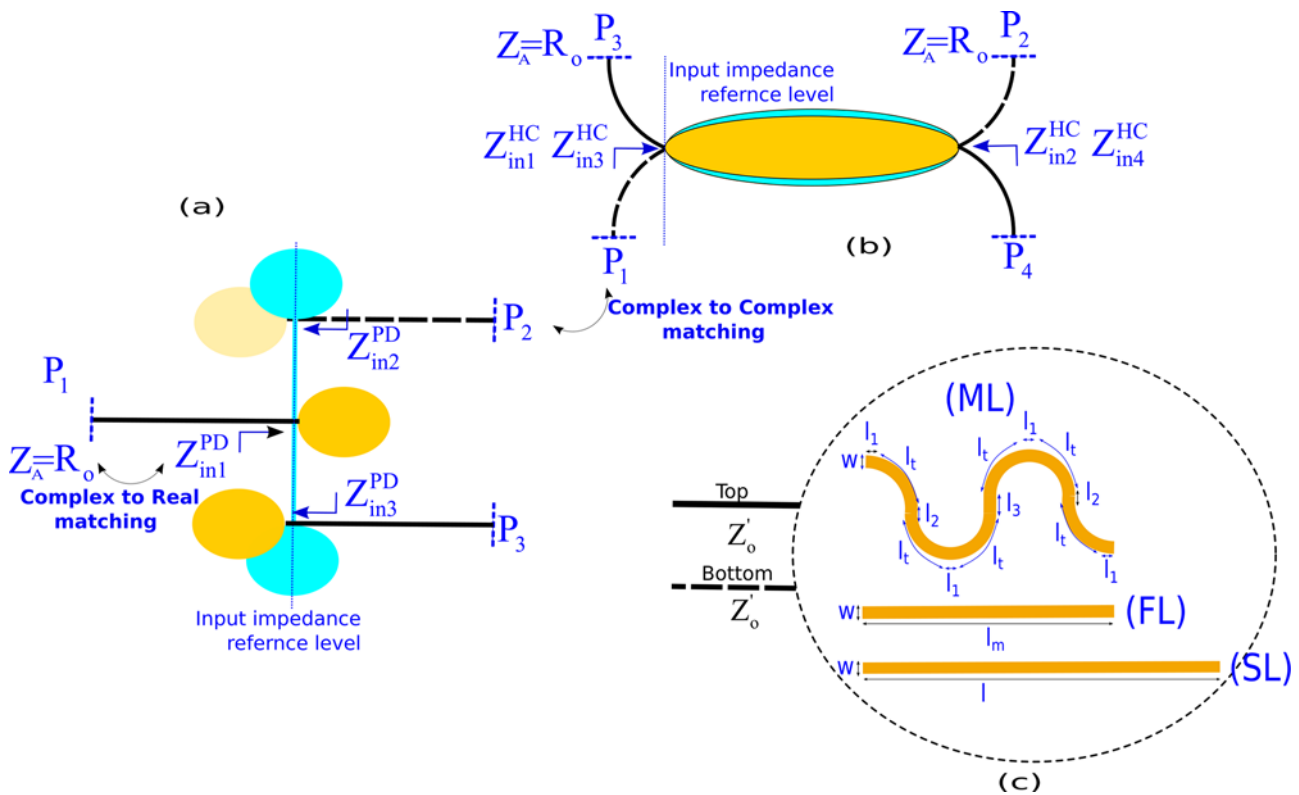


Figure 5. Wideband matching of multilayered HC and PD. (a) Power divider (PD), (b) hybrid coupler (HC), and (c) meander line (ML) used for matching.

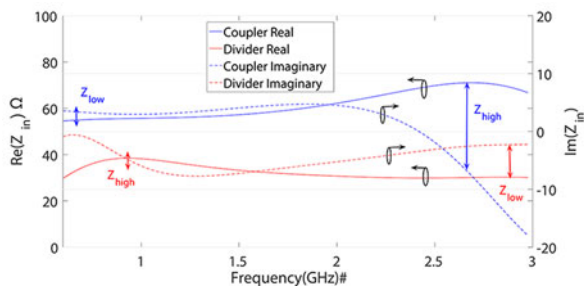


Figure 6. Input impedance versus frequency for HC ports and P-1 of the PD. The low (Z_{low}) and high (Z_{high}) impedances are denoted by arrows.

(and transform) a transmission line (to a Meander-one) to achieve not only hyperbolic means conjugate matching but also, and at the same time, band edge admittances compensation. Notably, the meander line acts in the same way as the series resonator but in a more compact form supporting miniaturization. In this way, it is easily understood that intermediate transmission line meandering results not only in the device’s miniaturization but also in wide band matching and as expected in BW improvement. This is the design approach that we contribute in the current work, and the major goal is to determine the optimal geometrical characteristics, width (W), and length (L) of the interconnecting lines between PD and HC of the SP junction. The proposed design provides the optimal performance of SP in terms of BW and q-points accuracy.

Having determined the core parameters of PD and HC as described in section “UWB multilayer power divider and 3 dB hybrid coupler,” the input impedance at the reference level

(shown in Fig. 5) of each port is provided (by simulation and measurements). In Fig. 5, Z_{in1}^{PD} , Z_{in2}^{PD} , and Z_{in3}^{PD} are the input impedances of the PD at the reference level for ports P_1 , P_2 , and P_3 , respectively. Z_{in1}^{HC} , Z_{in2}^{HC} , Z_{in3}^{HC} , and Z_{in4}^{HC} are the input impedances of the HC at the reference level for ports P_1 , P_2 , P_3 , and P_4 , respectively. Z_A is the complex impedance of the source (understood to provide power through the connectors), which is considered real, $Z_A = Z_o$. Due to the symmetry of HC’s and PD’s ports as shown in Fig. 5, it holds:

$$Z_{in1}^{HC} = Z_{in2}^{HC} = Z_{in3}^{HC} = Z_{in4}^{HC} \tag{9}$$

$$Z_{in2}^{PD} = Z_{in3}^{PD} \tag{10}$$

The input impedances of HC and PD ports at their reference level are shown in Fig. 6. As expected, due to the topology of the coupler similar to two parallel plates, its behavior is mostly capacitive. Referring to the HC, a low-quality factor parallel resonance appears at the high frequency band end (Fig. 6), but both the real and imaginary parts of Z_{in} present slow variations versus frequency. For mixer design, an optimal combination is a series transmission line section and a radial stub. The use of stub as mentioned earlier is avoided herein to retain a minimal footprint. However, as noted in [28], matching of a complex impedance to real Z_o can be achieved utilizing a single transmission line by properly adjusting both its characteristic impedance (defines the circular locus radius) and its electrical length ($\theta = \beta l$), which defines the circular arc length. Notably, a quarter wave transmission line ($\theta = \beta \lambda_g / 4 = 90^\circ$) could be approximately utilized to match only the real part $R_m = \text{Re}(Z_m)$ to Z_o (where Z_m denotes the hyperbolic mean impedance), but this does not take full advantage. Moreover, it is expected that the transmission line with smaller variation of

Table 2. Estimated hyperbolic mean of HC and PD (Fig. 5) for each of their ports

Device	P	Z _{low} (Ω)	Z _{high} (Ω)	Z _m (Ω)	Matching TL		Width (W) and length (L) (mm)			
					Z' ₀ (Ω)	θ' (deg)	W _{initial}	L _{initial}	W _{final}	L _{final}
HC	#1-4	54.5 + j3.5	71 - j7.7	61 - j6.5	56.98	62.38	0.91	17.4	1.02	18.3
PD	#1	29.7 - j0.8	38.4 - j4.8	33.8 - j2.5	41.00	79.3	1.4	21.7	1.37	20.9
	#2,3	15.9 - j14.6	108.6 + j0.4	41.8 - j12.6	46.29	60.9	1.26	16.8	1.1	16.5

the characteristic impedance versus frequency will offer an almost circular orbit with minimum radius on the smith chart, thus the smallest possible Voltage Standing Wave Ratio (VSWR). Following the above described approach, the hyperbolic mean impedance for the input port P₁ of the PD is denoted as:

$$Z_{m1}^{PD} = R_{m1}^{PD} + jX_{m1}^{PD} \tag{11}$$

while for the output ports P₂ and P₃ according to Equation (10) is:

$$Z_{m2}^{PD} = Z_{m3}^{PD} = R_{m2}^{PD} + jX_{m2}^{PD} \tag{12}$$

For the HC, since all ports have similar behavior, the hyperbolic mean impedance is identical at all ports:

$$Z_{m1}^{HC} = Z_{m2}^{HC} = Z_{m3}^{HC} = Z_{m4}^{HC} = Z_m^{HC} = R_m^{HC} + jX_m^{HC} \tag{13}$$

The real and the imaginary parts of the hyperbolic mean impedance in Equations (11), (12), and (13) can be calculated from the estimated (Fig. 6) Z_{low} = R_{low} + jX_{low} and Z_{high} = R_{high} + jX_{high} as [28]:

$$R_m = \left[R_{low}R_{high} \left(1 + \frac{(X_{low} - X_{high})^2}{(R_{low} + R_{high})^2} \right) \right]^{1/2} \tag{14}$$

$$X_m = \frac{X_{low}R_{high} + X_{high}R_{low}}{R_{high} + R_{low}} \tag{15}$$

Table 2 depicts the Z_{low}, Z_{high} and the estimated Z_m for each port of the HC and PD. The appropriate matching transmission line characteristic impedance and electrical length θ = βl are extracted herein through an algebraic manipulation of those given in [28–30]:

$$Z'_0 = \sqrt{\frac{\text{real}\{(Z_A^*Z_B^*)(Z_A - Z_B)\}}{\text{real}\{Z_A - Z_B\}}} \tag{16}$$

$$\tan(\beta'l) = Z'_0 \frac{|Z_A - Z_B|}{|Z_0'^2 - Z_A Z_B|} \tag{17}$$

Referring to Fig. 5, for the input port P₁ of the PD, a complex-to-real matching is applied since it is connected to 50 Ω connector; thus, Z_A = R₀ = 50 Ω and Z_B = Z_{m1}^{PD}. The same approach is applied to ports P₂ and P₃ of the HC Z_B = Z_m^{HC}. Output ports P₂ and P₃ of the PD are connected to HC ports, thus, a complex-to-complex matching is applied and the resulting characteristics of matching lines are given from Equations (16) and (17), with the corresponding hyperbolic mean impedances as Z_A = Z_{m2}^{PD} = Z_{m3}^{PD} and Z_B = Z_m^{HC}.

The matching process described so far involves only two components as shown in Fig. 5, yet the same process is followed for more interconnected components. Generally when a component is connected to a feeding port, a complex-to-real matching is applied, while a complex-to-complex matching is applied at the interstages when two components are connected to each other

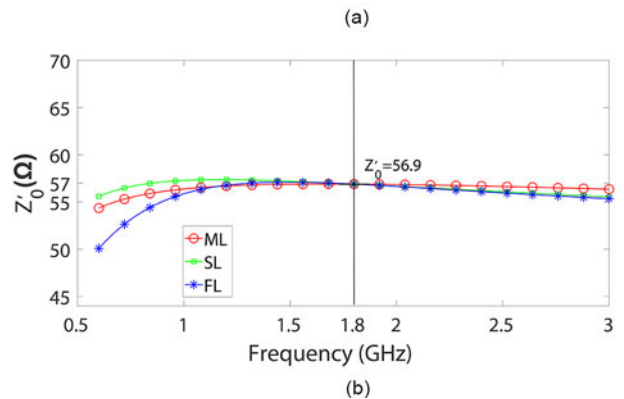
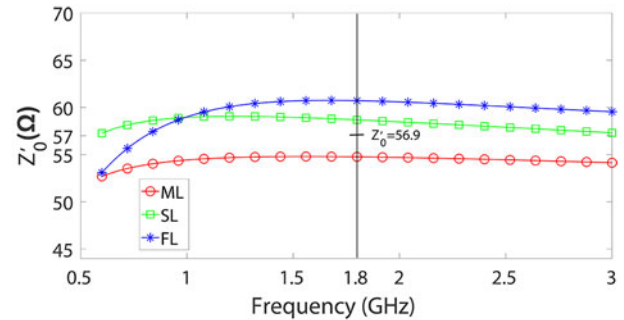


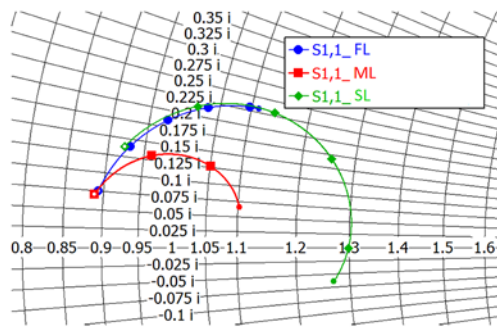
Figure 7. Characteristic impedance Z'₀ of the three line sections when W is (a) W = 0.91 mm (initial) and (b) W = 1.01 mm (fine-tuned in CST).

(e.g.) coupler-to-coupler or coupler-to-divider. After the calculation of the characteristic impedance Z'₀ and the electrical length θ' = β'l of the matched lines by Equations (16)–(17), the resulting W and L of the matching lines for each port of PD and HC are calculated from the well-known equations found in [40] and are depicted in Table 2. These lines are meandered in a smooth curved way, as shown in Fig. 5c, forming a miniaturized transmission line (ML). Also, for comparison, these are implemented by a straight line (SL), along with the straight line of the same footprint (FL), as the ML, also shown in Fig. 5c. The relation between the length of the SL and ML is given as:

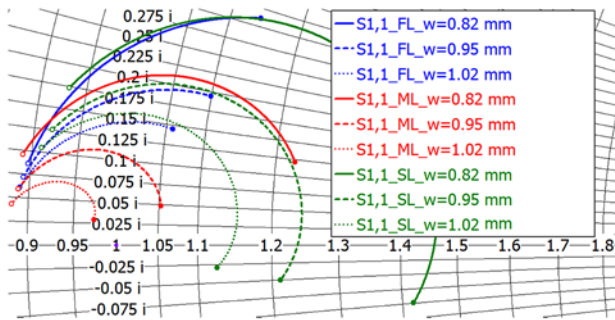
$$l = 6 \left[\sqrt{2}(l_t + w_m) \right] + 4l_1 + 2l_2 + l_3 \tag{18}$$

A CST simulation is utilized to accurately adjust the characteristic impedance and the electrical length of the three lines. Since CST offers only the S-parameters, these are transformed to ABCD, which reads as [40]:

$$\begin{bmatrix} A & B \\ C & D \end{bmatrix} = \begin{bmatrix} \cosh(\gamma'l) & Z'_0 \sinh(\gamma'l) \\ \sinh(\gamma'l)/Z'_0 & \cosh(\gamma'l) \end{bmatrix} \tag{19}$$



(a)



(b)

Figure 8. The Smith Chart locus for the input impedance of the three lines when width is (a) $W = 0.91$ mm and (b) $W = 0.82$ – 1.02 mm.

where $\gamma' = \alpha' + j\beta'$ and α', β' are the attenuation and phase constant, respectively. Notably, the constants α' and β' are approximately used for curved waveguides as the ML herein. Based on that, and after algebraic manipulation, the characteristic impedance can be calculated from in any case as

$$Z'_0 = \sqrt{\frac{B}{C}} \tag{20}$$

The electrical length can be directly estimated from the phase of its transmission coefficient $S_{21} = e^{-\gamma' l}$ as $\theta' = \beta' l = \text{Phase}(S_{21})$. Indicatively, for the coupler port-1, it is $Z_m = 61 - j6.5$ and Equations (16) and (17) yield $Z'_0 = 56.9 \Omega$, $\theta' = \beta' l = 62.4^\circ$. For Rogers 4003 Substrate ($\epsilon_r = 3.55$, $\tan \delta = 0.0027$, and thickness $h = 0.508$ mm), the corresponding W at the center frequency of 1.8 GHz is $w = 0.91$ mm and the required physical length $l = 17.4$ mm. Meandering this line, its footprint is reduced to $l_m = 8.4$ mm. In turn, the three lines are simulated in CST, and the resulting (by Equation 20) characteristic impedance is illustrated in Fig. 7(a), while their input impedance is shown in Fig. 8(a). The characteristic impedances (Fig. 7(a)) of SL and ML are different, and the SL is close to the designed ($Z'_0 = 56.9 \Omega$) while that of ML is about 2Ω lower. For the FL, Equation (20) depicts a wrong high variation of Z'_0 in Fig. 7(a), while Fig. 8(a) shows that its input impedance follows the correct track along to that of the SL. The width W of the three lines is fine-tuned within CST to yield the $Z'_0 = 56.9 \Omega$ at the center frequency as depicted in Figs. 7(b) and 8(b). From these, in particular, Fig. 8(b), it is obvious that the ML has the least variation in Z'_0 and the smaller diameter in its locus on the smith chart (Fig. 8(b)), thus better VSWR. A similar approach is followed to match the PD ports. These are in turn

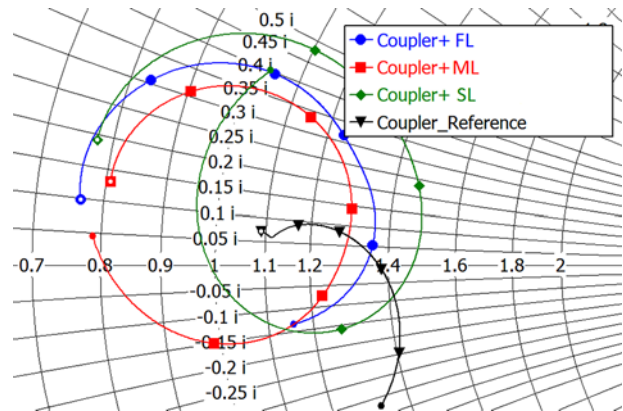


Figure 9. Input impedance locus on the Smith chart for the HC itself and the HC when the three different matching lines are attached to its ports as shown in Fig. 5.

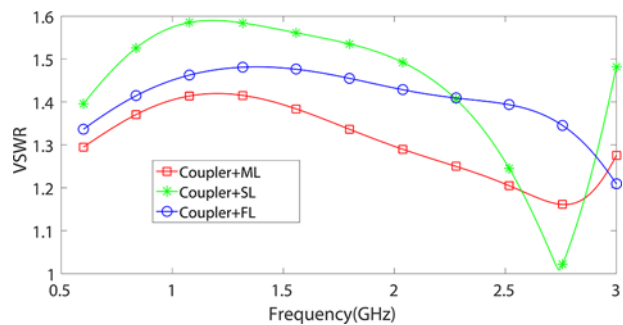


Figure 10. VSWR of the HC connected with the three different matching lines (Figure 5).

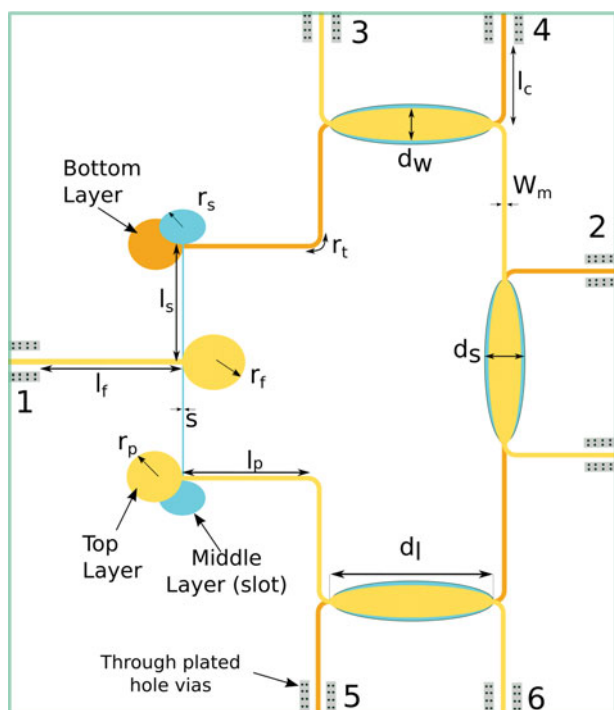
connected to the HC and PD (Fig. 5), and each structure is simulated using the CST. The resulting input impedance locus for the HC with the three different matching lines are shown in Fig. 9, while Fig. 10 depicts the corresponding VSWR. Both figures reveal the superior performance of the ML in term of both VSWR and miniaturization.

Summarizing, the steps for the implementation of the EBM approach combined with the new proposed smooth miniaturization scheme are as follows:

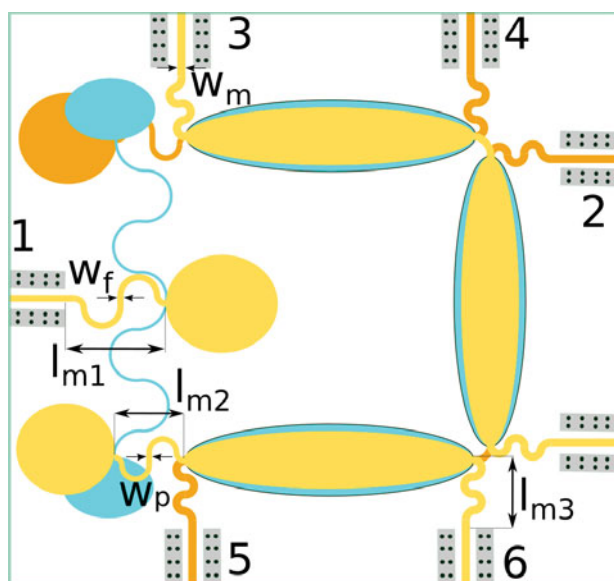
1. From the simulated S-Parameters, the real and the imaginary parts of Z_{in} at the reference ports of HC and PD are determined.
2. From Z_{in} , the hyperbolic mean impedances Z_m are calculated using Z_{low} and Z_{high} .
3. From Z_m , the characteristic impedance Z'_0 and the electrical length $\theta' = \beta' l$ of matched lines are calculated and subsequently, width (W) and length (L) of them are determined.
4. The resulting matching lines are meandered, and the ratio B/C is calculated and if necessary tuned to match Z'_0 . Final values for W and L are obtained.
5. The resulting MLs are connected to HC and PD ports to implement the SP junction.

Design and implementation of six-port networks

Following the design described in section “Extended broadband matching methodology of the hybrid coupler and power divider and footprint reduction,” two SP networks, covering the 0.6–3 GHz



(a)



(b)

Figure 11. Implemented (a) SL-SP and (b) ML-SP networks for the 0.6 to 3 GHz band. Dimensions (in mm): $l_{m1} = 11.6$ (actual 20.9), $l_{m2} = 8.6$ (actual 16.5), $l_{m3} = 9.2$ (actual 18.3), and $l_s = 19.1$ (actual 22).

band were implemented, as shown in Fig. 11. An SP using straight-lines (SL-SP) (Fig. 11(a)), with overall dimension $116 \times 102 \text{ mm}^2$ and a miniaturized SP using meander lines (ML-SP) (Fig. 11(b)), with overall dimensions of $68.2 \times 63.8 \text{ mm}^2$. The achieved size reduction is 63%, while the surface footprint of the layout is reduced to 37%, compared to the size of the SL SP. Both comprised three conductive layer interleaved with two dielectric layers.

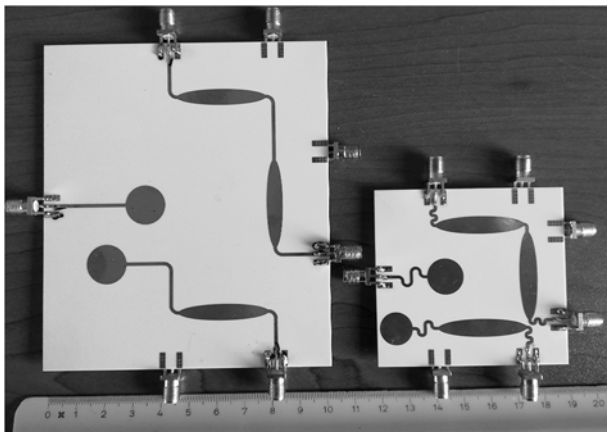
Table 3. Final values of the designed SP junctions.

Parameter (mm)	Fig. 11(a)	Fig. 11(b)
d_f	32.028	31.832
d_w	5.727	6.405
d_s	8.5	8.699
r_f	7	6.517
r_p	7	5.863
r_s	6	4.634
l_s	22	19
s	0.339	0.242
l_f	20.9	–
l_p	16.5	–
l_c	18.3	–
w_f	1.37	1.37
w_p	1.1	1.1
w_m	1.02	1.02
r_t	2.82	–

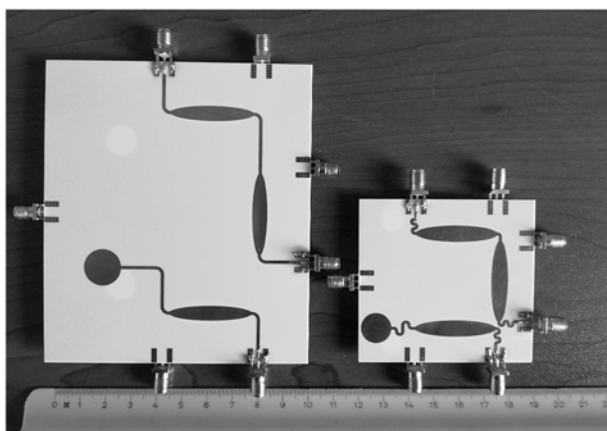
The top layer contains three conductive patches, connected to port 1 (feeding port) and to output ports 3 and 5. The bottom layer contains two conductive patches connected to port 2 (second feeding port) and to output ports 4 and 6. The middle layer contains the coupling region for PD and HCs slots. As depicted in Fig. 11, the SLs of the original SP (Fig. 11(a)) have been replaced by smoothed meandered sections having footprint lengths l_{m1} , l_{m2} , l_{m3} , and l_s (Fig. 11(b)). For a sufficient grounding of connectors and to minimize the parasitic effects, an extra 10 mm line and a 0.5 mm diameter through plated hole vias have been placed at each port as depicted in Fig. 11. The geometrical parameters relating the PD, r_f , r_p , r_s , s , and w_f , and HC, d_w , d_s , d_f , and w_p , of the SL-SP and ML-SP are shown in the second and third column of Table 3, respectively. The two fabricated SP prototypes operating in the 0.6–3 GHz band are shown in Fig. 12, with SLs (left) and with MLs (right). Each prototype is printed in two separated boards, which are glued back-to-back appropriately aligned and bonded together. For the bonding of SPs, 0.2 mm thickness (RO4450F) thin films have been used for the adhesion of the two Rogers4003C core layers.

Validation Results

In this section, the numerical results for the implemented SP networks are presented against the corresponding experimental results. The measurements have been done using HP8510C Vector Network Analyzer. The simulated and measured transmission coefficients for the ML-SP prototype of Fig. 12 (right) is presented in Fig. 13 when the excitation source is at port-1 (S_{i1} , $i = 3 - 6$) and in Fig. 14 when port-2 is excited (S_{i2} , $i = 3 - 6$). In both cases, there is a very good agreement between simulated and measured results. Since the input power is expected to be equally divided between these four outputs ports, the theoretical magnitude of these $|S_{i1}|$, $|S_{i2}|$ is expected at -6 dB . The observed values are fluctuating around -7 dB , with maximum deviation of $\pm 1.9 \text{ dB}$, over the range of 0.8–2.5 GHz. The 1 dB decrease of the mean value is due to the material losses ($\epsilon_r = 3.55$, $\tan \delta = 0.0027$) and to the



(a)



(b)

Figure 12. Constructed SL-SP (left) and ML-SP (right): (a) front view and (b) rear view.

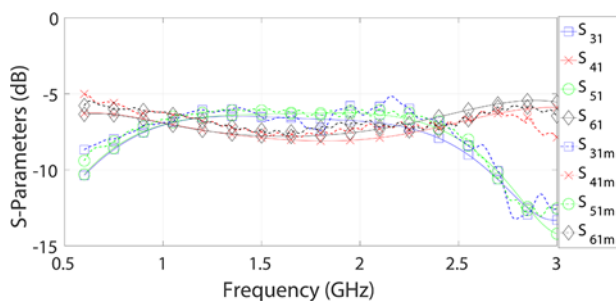


Figure 13. Transmission coefficients for the SP of Fig. 12 (right) when input port-1 is excited (S_{i1} , $i = 3 - 6$); subscript m denotes measurements.

manufacturing of the proposed networks, which results in tolerances when the layers were stacked. Even though alignment points were used, a tolerance of approximate $500 \mu\text{m}$ is expected. The simulated and measured VSWR of input ports 1 and 2 and output ports 3, 4, 5, and 6 is shown in Fig. 15. The maximum value of VSWR is 3.2 for port 3. The small band exceeding the limit of $\text{VSWR} \leq 2$ is restricted to the output ports, and it can be considered marginally acceptable. The relative phase shift at the output ports must be multiple of $\pi/2$ for an improved accuracy of the SP junction. In

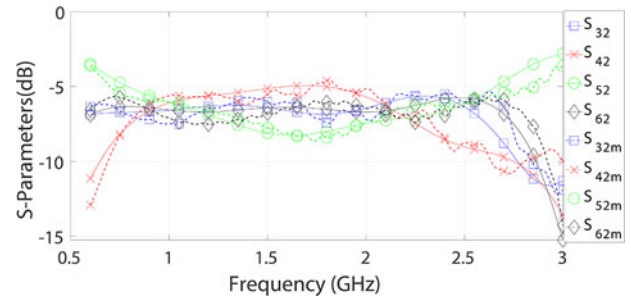


Figure 14. Transmission coefficients for the SP of Fig. 12 (right) when input port-2 is excited (S_{i2} , $i = 3 - 6$); subscript m denotes measurements.

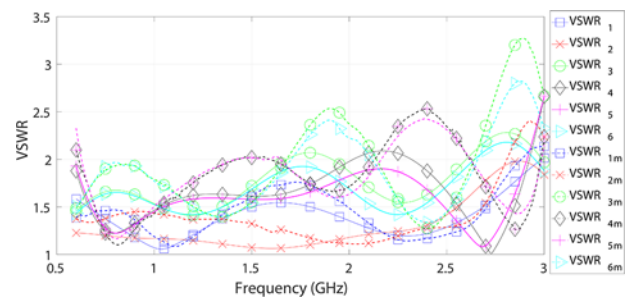


Figure 15. Simulated and measured VSWR of SP of Fig. 12 (right) for input ports 1 and 2 and output ports 3, 4, 5, and 6. Subscript m denotes the measurements.

Fig. 16, the phase response of the SP network is depicted when the two input ports 1 and 2 are excited. The relative phase differences are obtained comparing the phase response of output ports 3, 4, 5, and 6. Port 3 is used as reference port, consequently, ph_{34i} , ph_{35i} , and ph_{36i} denote the phase difference between port 3 and ports 4, 5, and 6, respectively. Subscript i denotes the excitation port ($i = 1, 2$). Hence, when port $i = 1$ is excited, these relative phase differences should be ideally $\Delta\phi_{34,1} = 90^\circ$, $\Delta\phi_{35,1} = 0^\circ$, and $\Delta\phi_{36,1} = 90^\circ$. When port $i = 2$ is excited, these relative phase differences should be ideally $\Delta\phi_{34,2} = -90^\circ$, $\Delta\phi_{35,2} = 90^\circ$, and $\Delta\phi_{36,2} = 0^\circ$. Figure 16 depicts the phase deviation of these relative phase differences from the ideal values. Indeed, these phase differences are close to the recommended, and there is a good agreement between simulated and measured phase responses. For the 0.8 to 2.5 GHz band, maximum phase deviation of 18° at 2.5 GHz and an average deviation of 7° is observed between ports 3 and 4 ($\Delta\phi_{34,2}$), while the average difference between the simulated and measured phase response of $\Delta\phi_{34,2}$ is 9.5° .

The magnitude and phase of q-points are presented in Figs. 17 and 18, respectively. As shown in Fig. 17(a) for the frequency band from 0.8 to 2.5 GHz, the magnitudes of q-points are in the range of 0.68–1.38 for the ML-SP and 0.75–1.38 for the SL-SP as shown in Fig. 17(b). Moreover for the whole range of operation (0.6–3 GHz), the magnitude of q-points varies from 0.5 to 3 for the ML-SP as shown in Fig. 17(a). Concerning the SL-SP, there is a significant deterioration beyond 2.7 GHz as shown in Fig. 17(b). Since ML provides hyperbolic mean conjugate matching and edge admittance compensation as noted in section “Extended broadband matching methodology of the hybrid coupler and power divider and footprint reduction,” as expected the ML-SP, as shown in Fig. 17(a), exhibits better performance in terms of q-point accuracy compared to the SL-SP and consequently offers an improvement of the operating BW. Regarding their phase separation, as

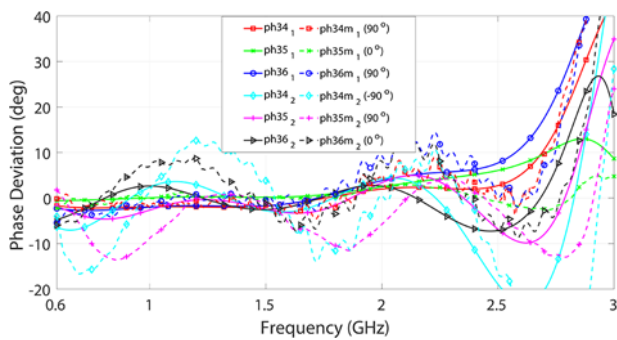
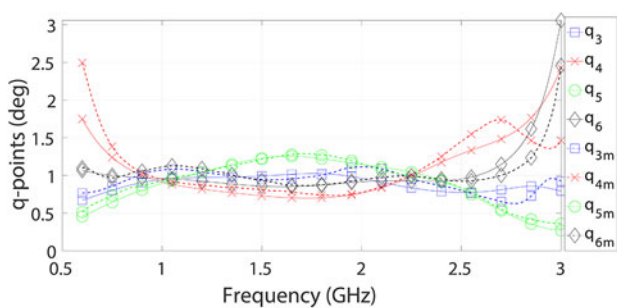
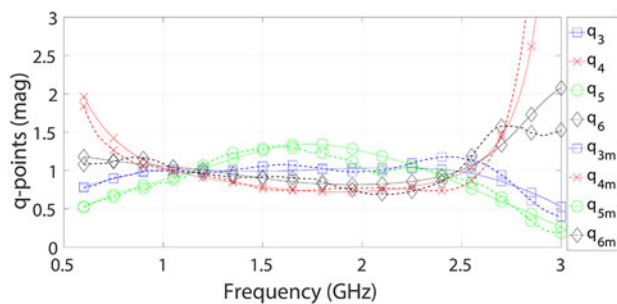


Figure 16. Phase deviation of the relative phase differences of the SP of Fig. 12 (right), for output ports 3, 4, 5, and 6 when ports 1 and 2 are excited ($ph3i_1, ph3i_m, ph3i_2, ph3i_m$). Subscripts i and m denote the excited and measurement's port, respectively. Ideal values for the phase differences are noted in the parentheses.



(a)

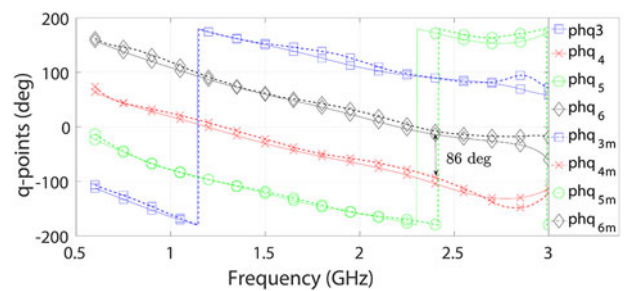


(b)

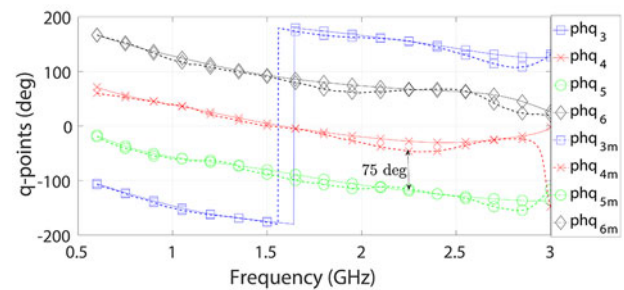
Figure 17. Simulated and measured magnitude of q-points for Fig. 17(a) ML-SP and Fig. 17(b) SL-SP. Subscript m denotes measurements.

shown in Fig. 18(a), for the ML-SP, it is equal to 90° with maximum deviation of -4° , where the ideal values is $\geq 90^\circ$. For the SL-SP (Fig. 18(b)), it is equal to 90° with maximum deviation of 15° . Additionally, a good agreement is observed between simulations and measurements.

Considering q-points as a performance metric, the ML-SP in Fig. 12 (right) according to the results presented so far is better in both magnitude and phase, compared with the results of the SL-SP in Fig. 12 (left). Although a reduction of dimensions to 63% and in volume down to 37% is achieved, the required performance and the UWV characteristics were preserved for the ML-SP network. Both structures exhibits sufficient performance over the 0.8–2.5 GHz frequency in terms of magnitude, phase response, and q-points accuracy. Comparing the ML-SP with the SP implemented with FL (not shown herein but available), again ML-SP exhibits better q-point accuracy.



(a)



(b)

Figure 18. Simulated and measured Phase of q-points for (a) ML-SP and (b) SL-SP. Subscript m denotes measurements.

Conclusion

A new design approach for multiport passive components is introduced. An extended and generalized wideband matching technique, combined with the new proposed miniaturization scheme, which employs a smooth curved meandering approach in both the microstrip and slotlines, achieved a size reduction of 63% for the ML-SP, compared to SL-SP, while retaining the same performance. The constructed SL-SP and ML-SP prototype networks exhibit the desired performance over the frequency range of 0.8 to 2.5 GHz.

Competing Interests. The authors report no conflict of interest.

References

- Engen GF (1977) The six-port reflectometer: An alternative network analyzer. *IEEE Transactions on Microwave Theory and Techniques* 25(12), 1075–108.
- Staszek K (2021) Balanced six-port reflectometer with nonmatched power detectors. *IEEE Transactions on Microwave Theory and Techniques* 69(11), 4869–4878.
- Chong C, Hong T and Huang K (2022) Design of the complex permittivity measurement system based on the waveguide six-port reflectometer. *IEEE Transactions on Instrumentation and Measurement* 71, 1–12.
- Morena-Álvarez-Palencia CD and Burgos-García M (2011) Four-octave six-port receiver and its calibration for broadband communications and software defined radios. *Progress in Electromagnetics Research-Pier* 116, 1–21.
- Ardakani MD and Tatu SO (2021) V-band six-port interferometer receiver: High data-rate wireless applications, BER and EVM analysis, and CFO compensation. *IEEE Access* 9, 160847–160854.
- Mirzavand R and Mousavi P (2018) A ZERO-power sensor using multiport direct-conversion sensing. *IEEE Sensors Journal* 18(22), 9243–9250.
- Arab H, Chioukh L, Ardakani MD, Dufour S and Tatu SO (2020) Early-stage detection of melanoma skin cancer using contactless millimeter-wave sensors. *IEEE Sensors Journal* 20(13), 7310–7317.

8. **Khalid N, Iyer AK and Mirzavand R** (2022) A batteryless six-port RFID-based wireless sensor architecture for IoT applications. *IEEE Internet of Things Journal* **9**(19), 18550–18558.
9. **Tatu SO, Serban A, Helaoui M and Koelpin A** (2014) Multiport technology: The new rise of an old concept. *IEEE Microwave Magazine* **15**(7), S34–S44.
10. **Cheong P, Tu M, Choi W-W and Wu K** (2022) An ingenious multiport interferometric front-end for concurrent dual-band transmission. *IEEE Transactions on Microwave Theory and Techniques* **70**(3), 1725–1731.
11. **Vinci G, Lindner S, Barbon F, Weigel R and Koelpin A** (2012) Promise of a better position. *IEEE Microwave Magazine* **13**(7), S41–S49.
12. **Jo H-W, Kim G, Kim K-S, Song C-H, Lee S-P, Kim E-K and Yu J-W** (2021) Accuracy-enhanced angle-of-arrival finding system using switched six-port network. *IEEE Antennas and Wireless Propagation Letters* **20**(2), 219–223.
13. **Yen H-C, Ou Yang L-Y and Tsai Z-M** (2022) 3-D indoor localization and identification through RSSI-based angle of arrival estimation with real Wi-Fi signals. *IEEE Transactions on Microwave Theory and Techniques* **70**(10), 4511–4527.
14. **Moghaddasi J and Wu K** (2020) Multifunction, multiband, and multimode wireless receivers: A path toward the future. *IEEE Microwave Magazine* **21**(12), 104–125.
15. **Ibrahim SZ, Abbosh A and Bialkowski M** (2012) Design of wideband six-port network formed by in-phase and quadrature Wilkinson dividers. *IET Microwaves, Antennas and Propagation* **6**(11), 1215–1220.
16. **Ibrahim SZ, Bialkowski ME and Karim MNA** (2012) Design of a fully integrated wideband six-port network on a single layer microstrip substrate. *Microwave and Optical Technology Letters* **54**(8), 1796–1803.
17. **Mohsin I, Karlsson M, Owais O and Gong S** (2013) Design and implementation of a UWB six-port correlator for 6–9 GHz frequency band. *Microwave and Optical Technology Letters* **55**(1), 190–193.
18. **Fang XT, Zhang X-C and Tong C-M** (2011) A novel miniaturized microstrip six-port junction. *Progress in Electromagnetics Research Letters* **23**, 129–135.
19. **Al-Areqi NN and You KY** (2018) Broadband and compact complex ratio measuring unit. *Microwave and Optical Technology Letters* **60**(12), 3039–3045.
20. **de la Morena-Álvarez-Palencia C, Burgos-García M and Rodríguez-Aparicio D** (2010) Three octave six-port network for a broadband software radio receiver. *The 40th European Microwave Conference*, Paris, France. New York City: IEEE.
21. **Peng H, Yang Z and Yang T** (2012) Design and implementation of an ultra-wideband six-port network. *Progress in Electromagnetics Research* **131**, 293–310.
22. **Li H, Zhu J and Li E.** (2017) A design of compact microwave six-port device for ultra-wideband applications. *Progress in Electromagnetics Research Letters* **65**, 57–61.
23. **Bialkowski ME, Abbosh AM and Seman N** (2007) Compact microwave six-port vector voltmeters for ultra-wideband applications. *IEEE Transactions on Microwave Theory and Techniques* **55**(10), 2216–2223.
24. **Abielmona S, Nguyen HV, Caloz C, Wu K and Bosisio RG** (2007) Compact multilayer ultra-wideband six-port device for modulation/demodulation. *Electronics Letters* **43**(15), 813–815.
25. **Winter S, Koelpin A and Weigel R** (2008) Six-port receiver analog front-end: Multilayer design and system simulation. *IEEE Transactions on Circuits and Systems II: Express Briefs* **55**(3), 254–258.
26. **Morena-Álvarez-Palencia CD, Burgos-García M and Gismeno-Menoyo J** (2013) Miniaturized 0.3–6 GHz LTCC six-port receiver for software defined radio. *Progress in Electromagnetics Research-Pier* **142**, 591–613.
27. **Tegowski B and A Koelpin** (2023) A compact stacked SIW six-port junction, *IEEE Microwave and Wireless Technology Letters* **33**, New York City: IEEE. 515–518.
28. **Bahl I and Bhartia P** (2003) *Microwave Solid State Circuit Design*, 2nd edn. New Jersey: Wiley.
29. **Clemetson WJ, Kenyon ND, Kurokawa K, Owen B and Schlosser WO** (1971) An experimental MM-wave path length modulator. *Bell System Technical Journal* **50**(9), 2917–2945.
30. **Packard H** (1980) Impedance matching techniques for mixers and detectors. Hewlett-Packard Co, Application Note 963.
31. **Abbosh AM and Bialkowski ME** (2007) Design of compact directional couplers for UWB applications. *IEEE Transactions on Microwave Theory and Techniques* **55**(2), 189–194.
32. **Bantavis PI, Kolitsidas CI, Empliouk T, Le Roy M, Jonsson BLG and Kyriacou GA** (2018) A cost-effective wideband switched beam antenna system for a small cell base station. *IEEE Transactions on Antennas and Propagation* **66**(12), 6851–6861.
33. **Xiao L, Peng H and Yang T** (2014) The design of a novel compact ultra-wideband (UWB) power divider. *Progress in Electromagnetics Research Letters* **44**, 43–46.
34. **Bialkowski ME and Abbosh AM** (2007) Design of a compact UWB out-of-phase power divider. *IEEE Microwave and Wireless Components Letters* **17**(4), 289–291.
35. **Xiao L, Peng H and Yang T** (2014) Compact ultra-wideband in-phase multilayer power divider. *Progress in Electromagnetics Research Letters* **48**, 33–37.
36. **Shuppert B** (1988) Microstrip/slotline transitions: Modeling and experimental investigation. *IEEE Transactions on Microwave Theory and Techniques* **36**(8), 1272–1282.
37. **Knorr JB** (1974) Slot-line transitions (short papers). *IEEE Transactions on Microwave Theory and Techniques* **22**(5), 548–554.
38. **Gupta KC, Garg R, Bahl I and Bhartia P** (1996) *Microstrip Lines and Slotlines*, 2nd edn. Norwood, MA: Artech House Publishers.
39. **Vincenti Gatti R and Rossi R** (2017) A novel meander-line polarizer modeling procedure and broadband equivalent circuit. *IEEE Transactions on Antennas and Propagation* **65**(11), 6179–6184.
40. **Pozar DM** (2011) *Microwave Engineering*, 3rd ed. New York: Wiley.



Chamber of Greece.



Communication and Knowledge, ENSTA-Bretagne, Brest, France, and the Université de Bretagne Occidentale, Brest. Currently, he is working with the project REVOLVE in partnership with Thales Alenia Space, Toulouse, France, and Prodintec, Gijon, Spain. His current research interests include lens antennas, antennas arrays, beamforming networks, and full-duplex systems.

Tzichat M. Empliouk received the Diploma and M.Sc. degrees in electrical and computer engineering from the Democritus University of Thrace, Xanthi, Greece, in 2004 and 2009, respectively, where he is currently pursuing the Ph.D. degree with the Microwave Laboratory. His current research interests include beamforming networks, antennas and antenna arrays, and six-port networks. Mr. Empliouk is a member of the Technical

Petros I. Bantavis received the Diploma degree in electrical and computer engineering from the Democritus University of Thrace, Xanthi, Greece, in 2016 and the Ph.D. degree from Institut d' Electronique et de Telecommunications de Rennes, Rennes, France. In 2015, he was a trainee with the KEMEA Center for Security Studies, Athens, Greece. He was with the Laboratory of Sciences and Techniques of Information,



Christos I. Kolitsidas received the Diploma and M.Sc. degrees (Hons.) in electrical and computer engineering from the Democritus University of Thrace, Xanthi, Greece, in 2008 and 2012, respectively, and the Ph.D. degree from the Department of Electromagnetic Engineering, KTH Royal Institute of Technology, Stockholm, Sweden, in 2017. In 2017, he was a Research Visitor with the Cavendish Laboratory, Cambridge University,

Cambridge, U.K. His current research interests include antennas and antenna arrays, beamforming networks, energy harvesting, SIW technology, lens antennas, and radio astrophysics for the Global Epoch of Reionization experiment. Dr. Kolitsidas was the Team Mentor and Project Leader of the team Trialectric in 2016. He was a recipient of the Best Student Paper Award in 2008 at the Mediterranean Microwave Symposium and in 2014 at the Progress in Electromagnetic Research Symposium and First Prize in the student design contest held in the IEEE Antennas and Propagation Symposium.



Theodoros N. F. Kaifas (Senior Member, IEEE) received the B.Sc. degree in Physics and the M.Sc. and Ph.D. degrees in electronic physics (Radioelectrology) from the Department of Physics, School of Science, Aristotle University of Thessaloniki (AUTH), Thessaloniki, Greece, in 2004. Since 1993, he has been a member of the Radio Communications Laboratory (RCL), Department of Physics, AUTH, where he has been

an Adjunct Professor for the Program of Postgraduate Studies in Electronic Physics since 2004. From 2001 to 2008, he was an Adjunct Professor with

the Department of Information and Electronic Engineering, International Hellenic University, Thessaloniki, Greece. He is currently an Assistant Professor with the Department of Electrical and Computer Engineering, Democritus University of Thrace (DUTH), Xanthi, Greece. He has a broad knowledge and experience in information technology and communications and an expertise in wireless communications, satellite communications, RF/microwave circuits, antenna analysis and design, and computational methods in electromagnetics.



George A. Kyriacou (Senior Member, IEEE) was born in Famagusta, Cyprus, in March 1959. He received the Electrical Engineering Diploma and Ph.D. degrees (Hons.) from the Democritus University of Thrace, Xanthi, Greece, in 1984 and 1988, respectively. Since January 1990, he has been with the Department of Electrical and Computer Engineering, Democritus University of Thrace, where he is currently a Professor and the Director

of the Microwaves Laboratory and was the Director of the Graduate Studies from 2005 to 2010. He has authored more than 250 journal articles and conference papers and supervised 8 Ph.D. and 15 M.Sc. theses and more than 110 Diploma theses. His main research interests include microwave engineering, open waveguides and antennas in anisotropic media, software defined and cognitive radio, computational electromagnetics, and biomedical engineering. Professor Kyriacou is a member of the Technical Chamber of Greece and the European Microwave Association.